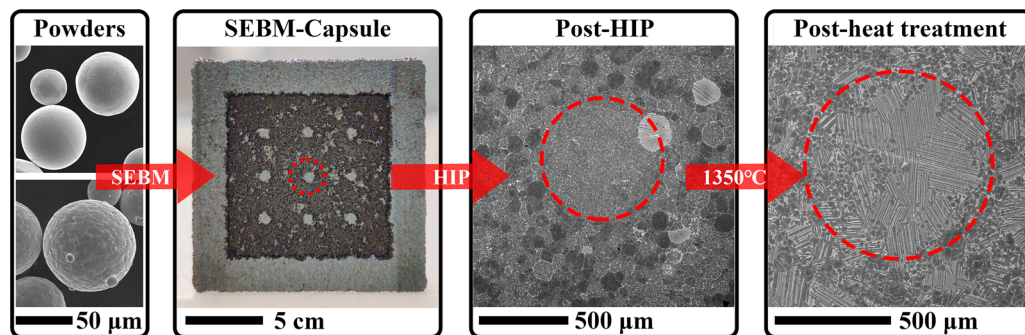


A Combined Powder Metallurgical Approach to Process Gamma-TiAl with Composite Structure



R. GAO, H. PENG, H. GUO, and B. CHEN

Gamma-TiAl (> 99 pct) sample with composite structural design was fabricated by a combined powder metallurgical approach of the SEBM capsule and HIP. Selective electron beam melting (SEBM) was used to create the pre-sintered powder bed, composite structure and the capsule, followed by hot isostatic pressing (HIP) at 1250 °C. A mixture of plasma rotating electrode (PREP) and gas atomization (AA) processed powders, with the respective higher (49.66 at. pct) and lower Al (47.61 at. pct) concentrations, was employed successfully to track the transition from powder to bulk sample, providing enriched information to elucidate the microstructure formation mechanism. The selective melting created composite structure consisted of the fine equiaxed γ -grains, while the rest of the powder bed that had been subjected to preheat only and then HIP was characterized by the triple microstructure. Formation mechanisms of such unique microstructure, consisting of primarily the coarse γ -grains and fine γ -grains with the previous particle boundaries (PPBs), were correlated to the Al concentration. The Al-rich powder was transformed into the coarse γ -grains, while the Al-depleted powder was responsible for the fine γ -grains with the PPBs. This finding suggests that the detrimental PPBs can be eliminated by increasing the Al concentration in the nascent powder. In the post-heat treated condition (1350 °C), no PPBs was found, suggesting that heat treatment is beneficial by eliminating the PPBs. For the designed composite structures, there was evidence to suggest desired distribution of the hard and soft regions, with the fine γ -grains associated with the composite structure being responsible for the high hardness region.



<https://doi.org/10.1007/s11661-022-06703-4>
© The Author(s) 2022

I. INTRODUCTION

THE solidification path, microstructure and resulting mechanical properties of TiAl alloy are highly dependent on the Al concentration.^[1] Selective electron beam melting (SEBM), a powder bed fusion additive manufacturing (AM), has created a great potential for processing TiAl since 2010,^[2] and a recent work has demonstrated its capability to fabricate turbine airfoils made of Ti-48Al-2Cr-2Nb.^[3] The chosen process parameters, in particular the beam condition in the melt stage, can strongly affect the Al concentration in the bulk sample (named as Al loss).^[4] The Al loss as

R. GAO and H. GUO are with the School of Materials Science and Engineering, Beihang University, Beijing 100191, China. H. PENG is with the Research Institute for Frontier Science, Beihang University, Beijing 100191, China. Contact e-mail: bo.chen@leicester.ac.uk B. CHEN is with the School of Engineering, University of Leicester, Leicester LE1 7RH, UK. Contact e-mail: penghui@buaa.edu.cn
Manuscript submitted October 24, 2021; accepted April 22, 2022.
Article published online May 7, 2022

reported in the previous SEBM work covers a wide spectrum from 0.3 to 8 at. pct.^[5–7] with the most frequent values ranging from 0.5 to 2 at. pct.^[1,4,8,9] Note that the Al loss in SEBM TiAl cannot be strictly prohibited for two reasons: (i) high saturated vapor pressure of Al when compared to Ti and Nb^[8]; (ii) its evaporation from the micro-melt pool into vacuum chamber is a continuous process since those gaseous Al would be condensed at the cold surface of heat shield.^[1,10] In addition, the Al distribution was inhomogeneous within the micro-melt pool.^[1] Therefore, strategy needs to be developed to minimize the Al loss in both the macroscopic and microscopic scales.

Inhomogeneous microstructure, with alternating layers of the duplex (often defined as the combination of lamellar α_2/γ colonies and equiaxed γ -grain) and γ -grain bands, arranged perpendicular to the build direction of SEBM TiAl, has been reported in References 4, 11–13. Mechanical properties can be altered by changing the angle of the band direction with respect to loading.^[4] Two different hypotheses have been proposed to explain the formation mechanism of the layered microstructure. The first group (e.g. Seifi *et al.*^[12] and Semiatin *et al.*^[14]) claimed that micro-segregation was inherited from the solidification of powder particles. This means that thermal transients into the single α -phase field that had been experienced by the already solidified layers would be too short (tens to hundreds of milliseconds^[8]) to create chemical homogenization that often requires the tens of minutes or hours of heat treatment.^[12,15] The second group (e.g. Todai *et al.*^[4] and Wang *et al.*^[16]) attributed the layered microstructure to *in-situ* heat treatment effect—the heat conduction from the top layer of the micro-melt pool would cause the areas beneath heat treated to different temperatures depending on their vertical distances.^[4,17] Without the consensus about how the layered microstructure was developed, it would be difficult to adopt appropriate strategy to achieve homogeneous microstructure.

The TiAl alloy fabricated by other powder metallurgy (PM) approaches such as hot isostatic pressing (HIP) or spark plasma sintering (SPS), where the powder feedstock was used as the starting material,^[18] often encountered a shell-structure phenomenon characterized by the previous particle boundaries (PPBs).^[19–22] The PPBs are detrimental to mechanical properties of TiAl alloy,^[20] primarily due to the nano-scale oxide layer of 10 nm thick appearing at the surface of powder particles.^[19] Oxygen is a strong α -phase stabilizer and its enrichment in α_2 -phase can reach the concentration of 10 to 20 at. pct.^[23] This is consistent with the observed phase constitution in the PPBs that consist of α_2 or lamellar α_2/γ colonies. Note that the oxygen pick-up is inevitable especially for the highly active TiAl melt, regardless of the powder production method. Also, the HIP powder filling step does not help to reduce the oxygen pick-up.

One way to address above-mentioned shortcomings is to combine SEBM with HIP, as attempted by Bieske *et al.*^[21] In that work, the SEBM capsule technology that involved firstly creating the enclosed capsule *via* the SEBM under vacuum, and secondly employing HIP to

fully densify the powders, was used to fabricate TiAl samples. Note that the PPBs still appeared in the post-HIP condition and this was attributed to the Al loss induced by the SEBM preheat step.^[21] This forms the first goal of the present work that is to elucidate the formation of PPBs in TiAl alloy processed *via* SEBM capsule technology. The second goal is to explore the composite structural design concept to realize microstructure tailoring at sample dimension by employing the SEBM capsule technology. This holds the promise in achieving a balanced strength and room temperature ductility in TiAl alloy by introducing soft γ -grains in the specific region to promote the synergistic deformation.^[4]

II. MATERIAL AND EXPERIMENTAL

A. Sample Fabrication

A mixture of plasma rotating electrode processed powders (PREP, with higher Al) and Ar gas atomization processed ones (AA, with lower Al) with nominal composition of Ti–48Al–2Cr–2Nb (all in atomic percent, unless otherwise stated) were purposely chosen in the present work for a twofold reason: first, elucidating the effect of Al concentration on the formation of PPBs under the same pre-heat parameters; second, maintaining the SEBM process stability.

Figure 1(a) shows a schematic diagram of the vertical and horizontal planes of the SEBM capsule with an overall dimension of $16 \times 16 \times 50 \text{ mm}^3$. The red area indicates the dense capsule with a wall thickness of 2 mm, created by the SEBM melt step, while the grey area indicates the powder bed inside the capsule. The top and bottom parts of the capsule are 5 mm in height. Three types of composite structures, named as pillar (Figure 1(b)), wafer (Figure 1(c)) and partial-melt (Figure 1(d)), were designed in the interior of the SEBM capsule.

Four samples were built per composite structure in the same batch using an Arcam A2XX machine with Control Software 3.2. All samples were built on the top of a stainless-steel starting plate ($\Phi 155 \times 20 \text{ mm}$) within the central area of $100 \times 100 \text{ mm}$, with layer thickness and hatch depth selected as $90 \mu\text{m}$. A thermocouple was attached to the bottom of the plate to measure the build temperature ($\sim 1050 \text{ }^\circ\text{C}$). The whole SEBM fabrication was carried out under the vacuum pressure of 1 Pa with high-purity helium (Helium 5.0) used as regulating gas. In practice, the build chamber was pumped to 1×10^{-3} Pa to reduce the oxygen level, which was followed by regulating to 1 Pa using helium gas. Thereafter the chamber pressure was controlled under dynamic equilibrium by pumping out or injecting the helium. The process parameters summarized in Table I cover (i) pre-sinter step for preventing the smoke phenomenon, (ii) two preheat steps for maintaining the high build temperature and continue preventing smoke, and (iii) melt parameters for the capsule, pillar, wafer and partial-melt structures, respectively. More SEBM process information can be found elsewhere.^[3,24,25]

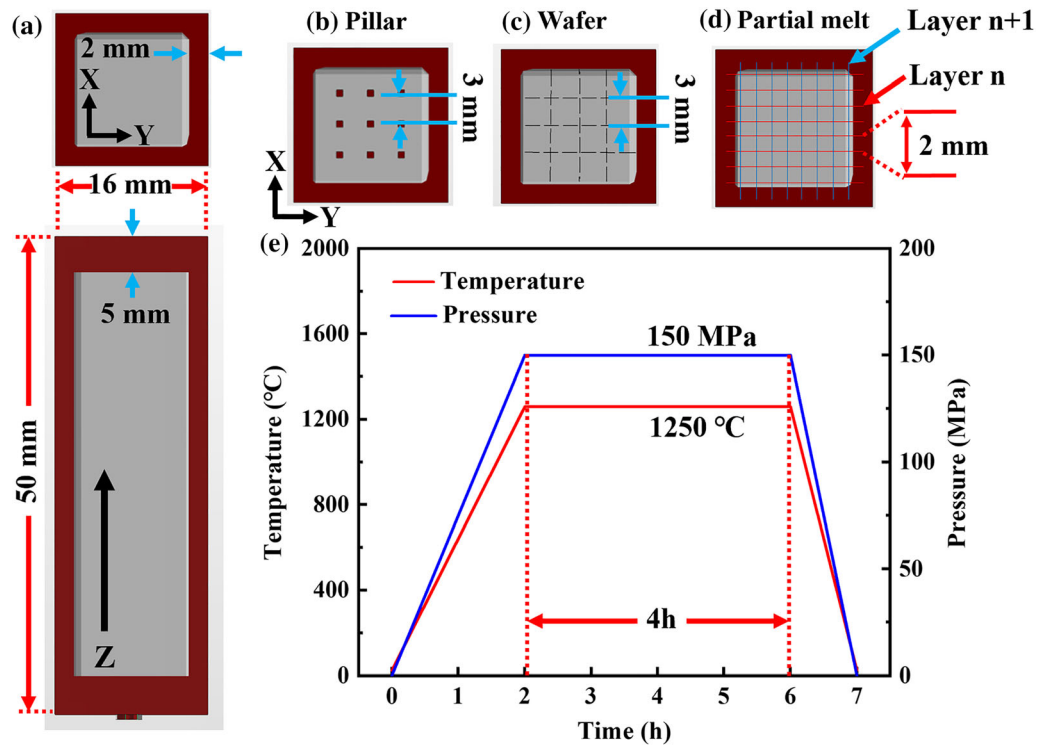


Fig. 1—Schematics of the SEBM capsule technology and *in-situ* composite structural concept: (a) vertical and horizontal cross-sections of the SEBM capsule; (b) to (d) the pillar, wafer and partial-melt composite structures; (e) temperature and pressure profiles during the HIP.

Table I. SEBM Process Parameters

Steps	Beam, mA			Scan Strategy	
	Focus Offset	Maximum Current	Average Current	Scan Speed (mm/s)	Line Offset (mm)
Pre-sinter	40	20	5	10,000	0.3
Preheat 1	150	35	28	10,000	1
Preheat 2	150	45	30	10,000	1
Capsule	0	10 ^a		1200	0.2
Pillar	0	1.7 ^a		500	—
Wafer	0	10 ^a		2000	—
Partial-melt	0	10 ^a		1200	2

^aA fixed beam current was used for fabricating the capsule, wafer, pillar and partial-melt structures. Thus, the value of maximum current equals the average current.

In terms of the pillar structure, 9 pillars with interspacing of 3 mm were built inside the capsule from the bottom to top (*i.e.* 40 mm tall), having each pillar dimension of $1 \times 1 \text{ mm}^2$ within the X - Y plane, Figure 1(b). In terms of the wafer structure, two groups of intersecting wafers (black dash lines in Figure 1(c)), parallel to the Z -build direction, were designed with the wafer interspacing set as 3 mm. This led to a square divided into 16 parts with each dimension of $3 \times 3 \text{ mm}^2$, printed using a scan speed of 2000 mm/s and beam current of 10 mA (Table I). For the partial-melt structure, it was built alongside the capsule using the same scan speed of 1200 mm/s (Table I). The primary difference between the two is that the partial-melt part was processed using a 10 times greater line offset of 2 mm and the contour melt was off. The selected line offset

was much larger than the width of the individual scanline (about $400 \mu\text{m}$ according to the micro-melt pool observation and process simulation^[8,13,24]). With the 90 deg beam rotation on, scanlines crossed each other for every adjacent layer as indicated by the red and blue lines in Figure 1(d). This was supposed to create a network structure inside the capsule in three-dimensional space.

Upon completion of the SEBM capsule and *in-situ* composite structural design, the enclosed samples were subjected to HIP in a Quintus QIH-9 HIP system to realize densification. Samples were heated to 1250 °C with a rate of 10 °C/min and the 150 MPa pressure was obtained by pumping high-purity argon (Argon 5.0) into the system, Figure 1(e). The samples were kept at 1250

°C for 4 hours, followed by furnace cooling to room temperature.

Heat treatment was performed using a calibrated GSL-1600X tube furnace in a dynamic argon atmosphere (Argon 5.0) with a flow rate of 220 mL/min. The post-HIP samples were heat treated at 1350 °C for 30 minutes and then furnace cooled to 950 °C under a rate of 10 °C/min. This was followed by a 30 minutes hold at 950 °C to minimize the possibility of cracking. Finally, samples were furnace cooled to 750 °C and then air cooled to room temperature.

B. Characterization Methods

1. Powder characterization

Five powder conditions were characterized to help understand the microstructure evolution from the powder to fully densified parts: the mixed powder, recycled powder, sieve residues, post-HIP and post-heat treated (post-HT) powders. The mixed powder was used as the reference condition. After each SEBM machine cycle, the sintered 'powder cake' was treated in the powder recovery system (PRS). And the powders left in the build chamber, as well as those in the hopper, were then collected. After the PRS, these powders were mixed and then subjected to sieving (160 μm mesh sieve). After this step, two characteristic powder samples were collected, namely, the recycled powder (passing through the sieve) and sieve residues (failing to pass through). A similar powder handling procedure was adopted previously.^[26] Regarding the post-HIP and post-HT powder conditions (thermal history simulation, namely, without the high pressure), two enclosed SEBM capsule samples without the composite structure in the interior were heat treated at 1250 °C for 4 hours, and then one sample was further heat treated at 1350 °C for 30 minutes followed by step cooling. Both samples were then cut to allow collecting the powders from inside. This method was chosen, as opposed to heat treating the powders in an argon-gas sealed quartz tube, because all powders were found to evaporate to the inner surface of the tube when employing the latter method.

Powder morphology was characterized using a JEOL 6010 scanning electron microscope (SEM). This was followed by the cross-sectional observation using a Zeiss Gemini SEM 300 equipped with energy dispersive spectrometer (EDS). All EDS results, presented in the paper, were based on a high number of measurements, whenever applicable, to ensure the statistical rigor. The powder size distribution was determined by laser particle diffraction using a Bettersize 2600 analyzer. The chemical composition of powders was determined *via* inductively coupled plasma atomic emission spectroscopy (ICP-AES). X-ray diffraction (XRD) phase identification was performed using a Rigaku D/MAX 2200pc diffractometer with scan speed of 3 deg/min over the 2θ range from 30 to 70 deg.

2. Bulk sample characterization

Archimedes drainage method was used to measure the sample density in both the as-SEBM and post-HIP conditions. The reported value represents an average of

three individual measurements. The relative density was obtained using the theoretical density of 4.0 g/cm³.^[27] SEM metallography examination was made on the cross-section cut by wire electrical discharge machining, and then mechanical polished down to 1 μm diamond paste. Bulk sample conditions included as-SEBM, post-HIP and post-HT. Backscattered electron (BSE) imaging mode was used to enhance the phase contrast. XRD phase identification was performed on bulk samples in the post-HIP and post-HT conditions.

Microhardness (HV_{0.5}) mapping, with typically 13 by 26 points for the column and row, respectively, was performed on the post-HIP samples in accordance with the ASTM E92-17 using an Innovatest Falcon 500 Vickers hardness tester. Indents were made with load of 500 g and dwell time of 15 seconds, and the distance between indents (approx. 63 μm in length) was set as 400 μm to eliminate the interaction.

III. RESULTS

A. Powders

Powder size distributions of the PREP, AA and mixed powders are illustrated in Figure 2(a), with the values of D10, D50 and D90 for the mixed powder determined as 42.6, 81.3 and 142.0 μm , respectively. The large powders which failed to pass through the sieve were removed, resulting in the shift of distribution curve towards the smaller size range, when compared to the original PREP and AA powders. Chemical composition of the mixed powder was determined as Ti-48.41Al-1.96Nb-1.97Cr (conforming to the Ti-48Al-2Cr-2Nb type), Figure 2(b). The PREP powder had a composition of Ti-49.66Al-1.89Nb-2.00Cr (higher Al) while the AA one had a composition of Ti-47.61Al-2.00Nb-1.97Cr (lower Al).

Representative SEM micrographs of the PREP and AA powders with spherical shape are shown in Figures 2(c) and (d), respectively, while their cross-sectional views are shown in Figures 2(e) and (f). The brighter contrast particle exhibiting coarse dendritic microstructure (red dotted circle, Figure 2(f)) was judged as the AA powder for two reasons: first, the presence of hollow powder due to gas atomization process,^[28] and second, the low Al being consistent with the brighter contrast under BSE imaging mode. By comparison, the darker contrast particle was PREP powder due to its higher Al concentration. XRD spectra in Figure 3 reveal that the AA powder mainly consisted of α_2 -phase while the PREP powder contained a similar amount of the α_2 - and γ -phases. The mixed powder consisted of 67 pct α_2 -phase and 33 pct γ -phase.

For the recycled powder, its composition was determined as Ti-48.38Al-1.93Nb-2.00Cr, showing virtually no difference when compared to the mixed powder (Ti-48.41Al-1.96Nb-1.97Cr). The particle size increased by 5.2, 8.7 and 14.2 pct in terms of the respective D10, D50 and D90 values. This can be attributed to the pre-sinter and preheat steps which caused small particles sintered with each other. Also, the

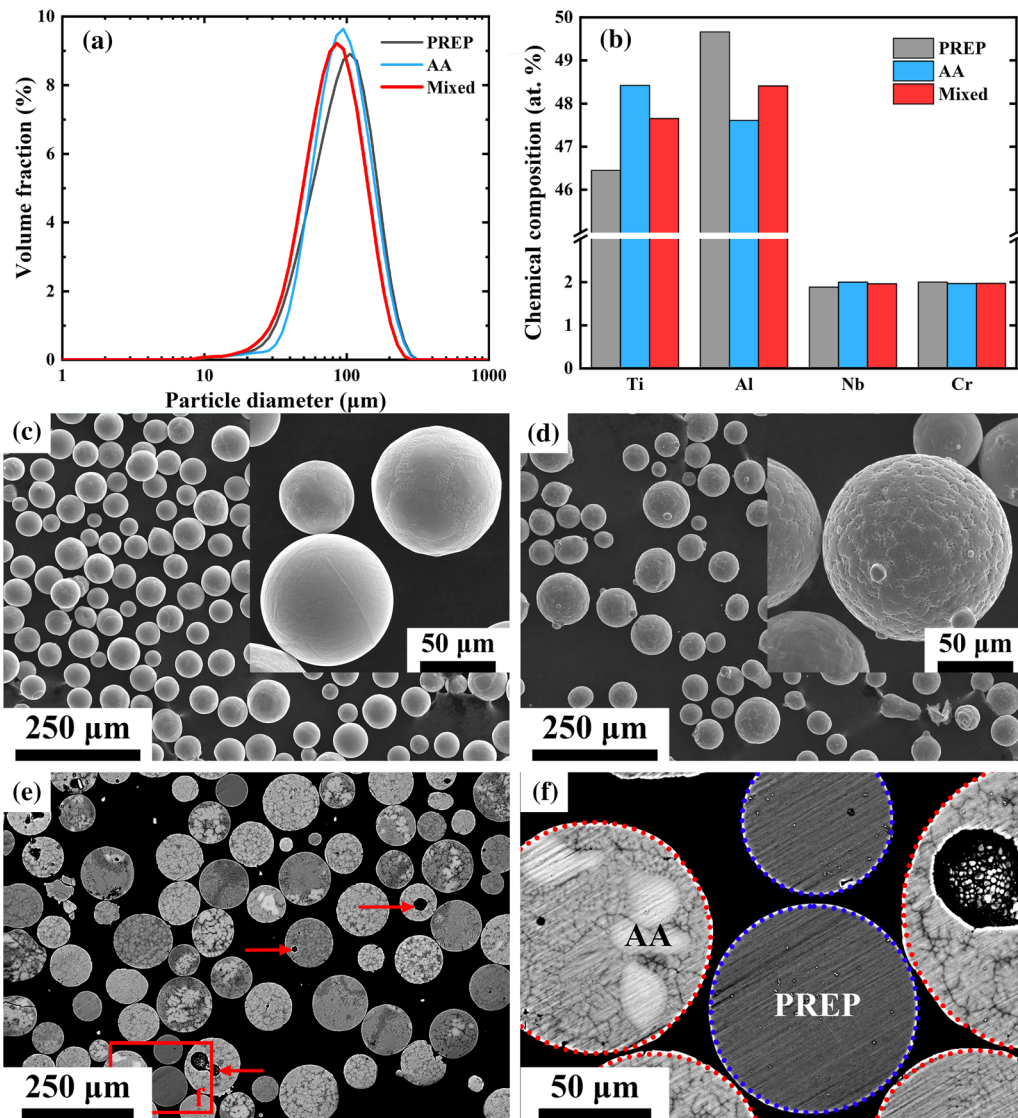


Fig. 2—The mixed powder: (a) and (b) particle size distribution and chemical composition of AA, PREP and mixed powders; (c) and (d) SEM micrographs of the powder morphology for the PREP and AA, respectively; (e) SEM cross-sectional view of the mixed powder with red arrows indicating the pores; (f) enlarged view of (e) revealing the characteristic feature of PREP and AA powders (Color figure online).

recycled powder had a much higher γ -phase fraction (85 pct) by comparison with the mixed powder (33 pct). This aligns with the non-equilibrium nature of as-processed powders; the thermal history experienced during the SEBM machine cycle triggered the $\alpha \rightarrow \gamma$ phase transformation, creating the equilibrium condition of γ -TiAl with the predominant γ -phase. Figure 4 shows the SEM cross-sectional view of the sieve residuals, showing two individual powders in semi-sintered condition. The region in-between was characterized by the fine grains near the powder boundary while coarse grains away from it. The Al content was measured as 37.49, 44.52, 46.80 and 39.33 at. pct, from locations 1 to 4 of Figure 4, indicating Al depletion near the powder boundary, while Al enrichment away from it.

Figures 5(a) and (b) present the typical microstructure of the post-HIP condition (1250 °C for 4 hours), and the EDS determined Al concentration is summarized in

Figure 5(e). Two different powder characteristics can be seen in Figure 5(a), with one revealing coarse γ -grains marked by the blue circles, while the other showing fine γ -grains marked by the red circles. The PPBs consisting of α_2/γ lamellar colonies, appeared near the powder surface, Figure 5(b). The coarse γ -grain powders (numbered from 1 to 10) always had a higher Al of 48.7 ± 0.3 at. pct, when compared to the fine γ -grain powders (numbered from 11 to 18) having lower Al of 46.9 ± 0.4 at. pct, Figures 5(a) and (e). The observed trend is consistent with the Al difference in the nascent powders with 49.66 at. pct for PREP while 47.61 at. pct for AA. Thus, the coarse γ -grain powders can be inferred as the PREP powder, while that characterized by the fine γ -grains was the AA powder.

For the post-HT condition (1250 °C for 4 hours, and then 1350 °C for 30 minutes), powders were characterized by two microstructure types, with one consisting of

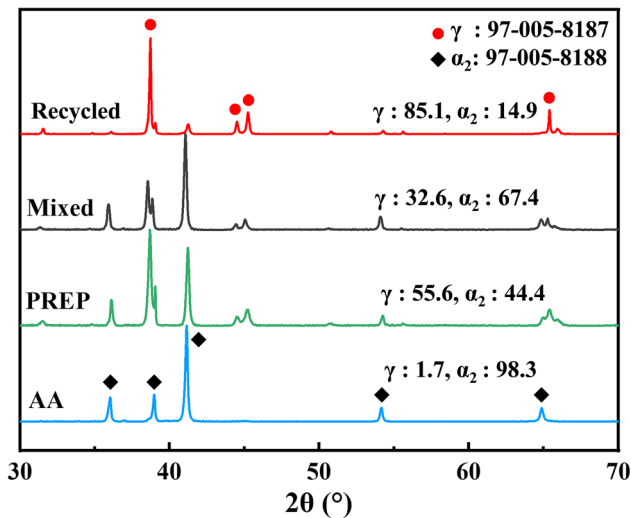


Fig. 3—XRD spectra of the powders in AA, PREP, mixed and recycled conditions.

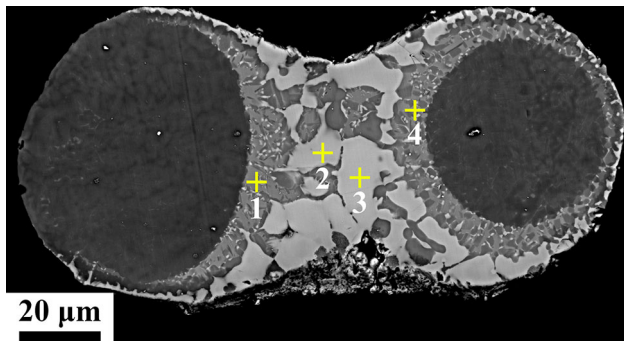


Fig. 4—SEM cross-sectional view of sieve residues including two powders and the EDS point analysis locations.

coarse γ -grains and the other composed of α_2/γ lamellar colonies, as indicated by blue and red circles in Figures 5(c) and (d), respectively. The coarse γ -grain powders (numbered from 1 to 4) had a consistently higher Al of 48.1 ± 0.5 at. pct, while the α_2/γ lamellar powders (numbered from 5 to 8, Figures 5(c) and (f)) had a lower Al of 46.3 ± 0.3 at. pct, suggesting that the former was the PREP powder while the latter was the AA one.

B. Post-HIP Condition of The Bulk Sample: SEBM Capsule vs. Inner Area

Table II compares the relative density in the as-SEBM and post-HIP conditions. Depending on the *in-situ* composite structural design, the as-SEBM samples had a different relative density, with the partial-melt one having the highest value (3.33 g/cm^3 in absolute density and 84.0 pct in relative density) among the three. After the powder densification *via* HIP, the relative density of samples increased considerably to greater than 99 pct as expected. This level of densification is as good as that found in post-HIP Ti-6Al-4V (97.2 to 99.7 pct).^[29,30]

The inner area exhibited a completely different microstructure when compared to the capsule, Figure 6(a). The capsule area that had been melted by the electron beam was characterized by a fine-grained equiaxed microstructure (Figure 6(b)), which is consistent with the SEBM TiAl in the post-HIP condition.^[12] By contrast, the inner area formed by the powder bed densification *via* HIP, exhibited three characteristic features as indicated by red circle in Figure 6(c), as well as blue and yellow circles in Figure 6(d). First, the red circle highlighted microstructure was characterized by the fine γ -grains surrounded by PPBs. Their diameter was measured as $124.9 \pm 22.5 \mu\text{m}$, which is not too far from the particle size of the mixed powder (D50 value of $81.3 \mu\text{m}$). Second, the blue circle highlighted microstructure in Figure 6(d) was characterized by the coarse γ -grains. Unlike the fine γ -grains, there was no PPB surrounding the coarse one. Within the inner area, the volume fraction of fine γ -grains was measured to be 57.0 pct, which is higher than that of 40.7 pct for the coarse γ -grains. Third, the yellow circle highlighted region in Figure 6(d) was characterized by the α_2/γ lamellar colony. Such microstructure feature had a considerably low volume fraction of 2.3 pct and its distribution within the inner area was random. The lamellar colony size was measured to be $233.5 \mu\text{m}$, which is significantly larger than the D90 value of the mixed ($142.0 \mu\text{m}$) and recycled ($162.1 \mu\text{m}$) powders.

To understand the Al evaporation, EDS was performed to obtain the chemical composition in the capsule and inner areas, Figure 7(a). The capsule area that had been melted by the electron beam showed an Al concentration of 46.6 at. pct, whereas the inner area that had been subjected to the pre-sinter and preheat steps only showed an Al concentration of 47.5 at. pct, Table III. The Al loss was determined as 1.8 at. pct for the capsule while 0.9 at. pct for the inner area with reference to the mixed powder (48.41 at. pct Al in Figure 2(b)). This means that the SEBM capsule technology is effective in controlling the Al loss to a low level.

For the triple microstructure as observed in Figures 6(c) and (d), their area-average compositions determined by EDS, are presented in Figure 7(b) for the lamellar colony grains (yellow rectangle) and the coarse γ -grains (blue rectangle), and in Figure 7(c) for the fine γ -grains with PPBs. There was a depletion of Al and Nb in the lamellar colony grains with the concentration of 3.9 and 1.2 at. pct lower than those in the inner area, Table III. The average Al content in the fine γ -grains was 0.8 at. pct lower than the coarse γ -grains. In addition, the PPBs in the fine γ -grained microstructure, composed of several fine α_2 -grains, showed a clearly defined Al lean boundary, accompanied by the Cr enrichment, Figure 7(c). Nb was evenly distributed in the fine γ -grains, and thus not shown here for brevity.

C. In-situ Composite Structure

The microstructure evolution of the *in-situ* composite structure in the inner area can be understood by examining the before and after HIP conditions. The

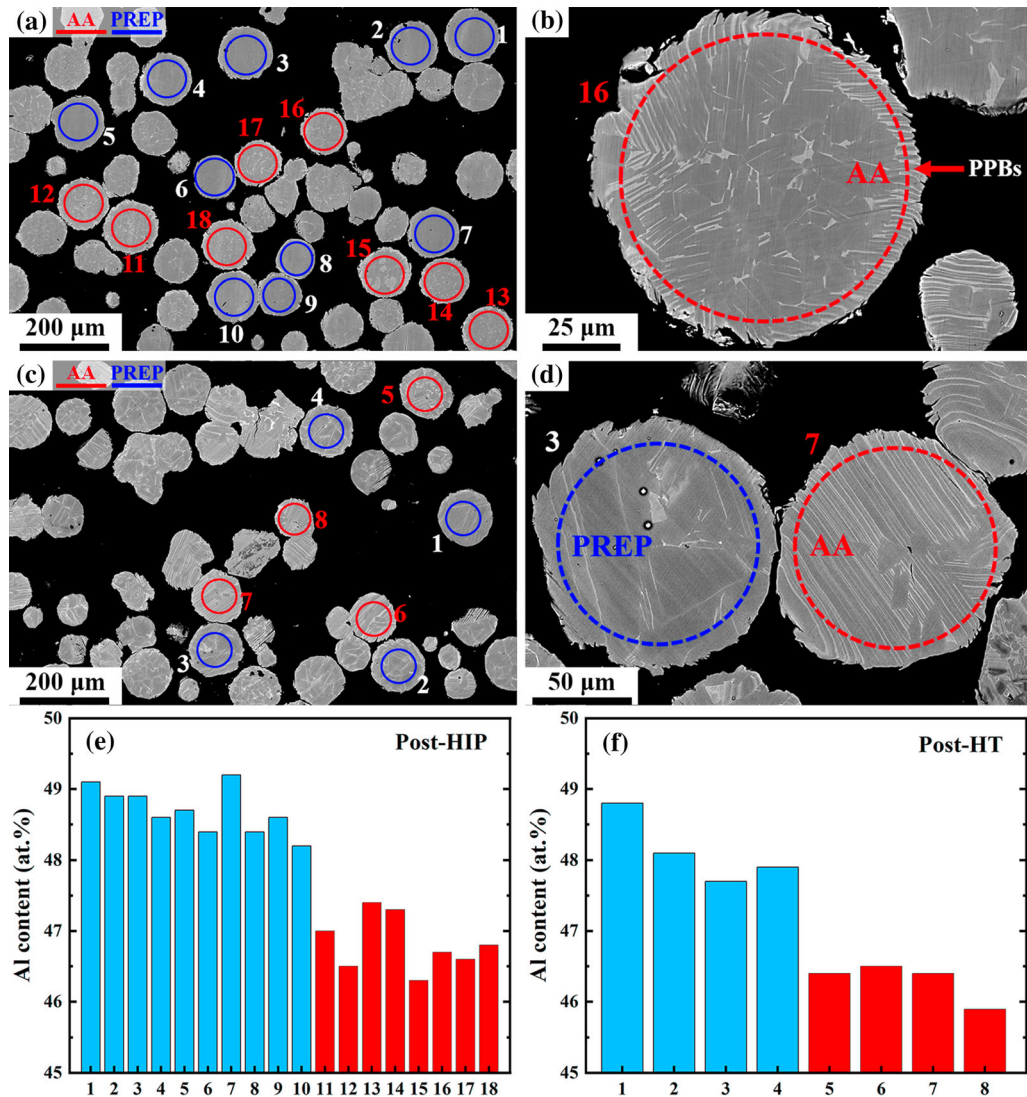


Fig. 5—SEM cross-sectional view of the post-HIP in (a) and (b) while post-HT powders in (c) and (d), with figures (b) and (d) illustrating the detailed powder microstructure. Circles in (a) to (d) indicate EDS analysis regions to determine the powder composition with the results summarized in (e) and (f).

Table II. Relative Density of Samples in As-SEBM and Post-HIP Conditions

Sample Condition	Relative Density (Pct)		
	Wafer	Pillar	Partial-Melt
SEBM	79.63	76.39	84.03
Post-HIP	99.35	99.66	99.50

pillar structure (Figure 8) is elaborated first, followed by the wafer (Figure 9) and partial-melt structures (Figure 10). Refer to Figures 1(b) through (d) for the *in-situ* composite structural design.

The cross-sectional view of the pillar structure in the as-SEBM condition is shown in Figure 8(a), where red arrows indicate the capsule, powder bed and pillar regions, respectively. The pillar structure was

successfully built with an interspacing distance of 3 mm. One of the pillars together with its surrounding powder bed is shown in Figure 8(b), where several partially molten powders were attached to the pillar, forming a consolidated chunk with a diameter of 732.5 μm . After HIP, the boundary between the pillar and densified powder bed was visible, see the red dash circle in Figure 8(c). The pillar microstructure in the post-HIP condition was characterized by the fine equiaxed γ -grains (grain size of $10.5 \pm 6.6 \mu\text{m}$) having the volume fraction of 94.0 pct, Figure 8(d). In addition, the irregular α_2 -grains were distributed at the γ -grain boundaries. Both the γ -grain size and its volume fraction were similar to the capsule area ($7.5 \pm 4.4 \mu\text{m}$, 86.3 pct). The γ -grain size agrees reasonably well with the SEBM TiAl under post-HIP condition,^[12] where the γ -grain size ranged from 4.4 to 20.4 μm . Compared to its surrounding powder bed (47.5 at. pct, inner area in Table III), the Al concentration was measured to be 46.8 ± 0.4 at. pct

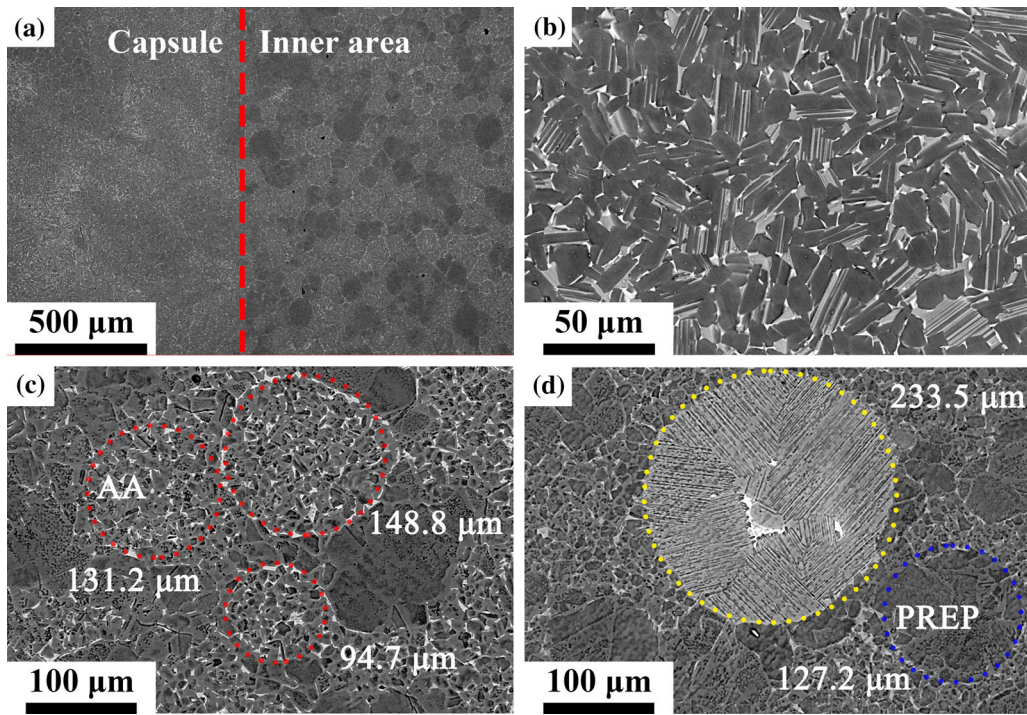


Fig. 6—SEM micrographs of the post-HIP sample prepared *via* SEBM capsule technology: (a) different microstructures as revealed in the capsule and inner areas; (b) detailed microstructure of the capsule area; (c) and (d) detailed microstructure of the inner area with the red, yellow and blue dotted lines indicating three typical features (Color figure online).

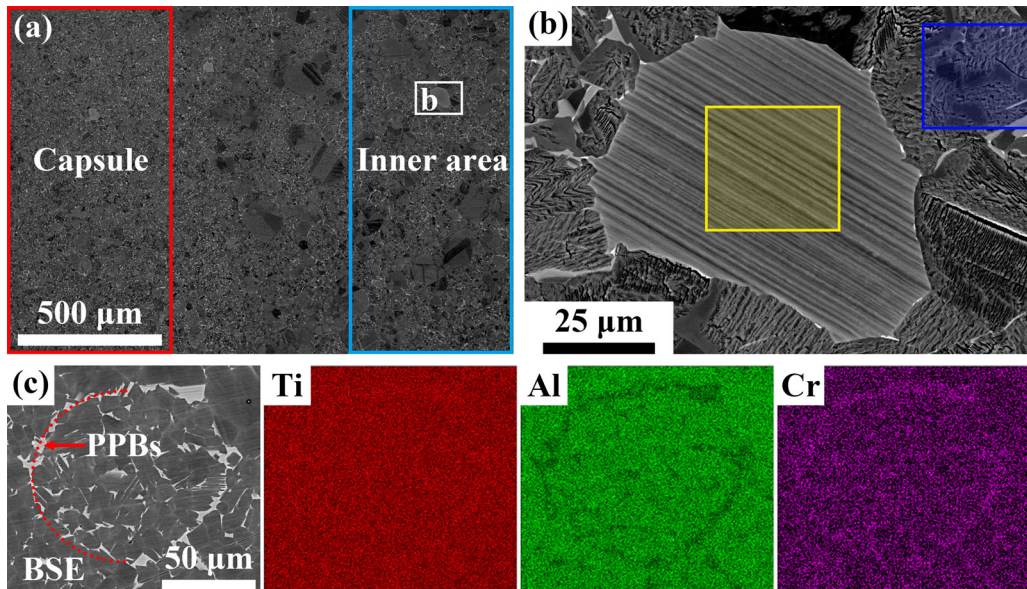


Fig. 7—SEM + EDS results of the post-HIP sample: (a) SEM micrograph showing the boundary of the capsule and the inner area with red and blue rectangle indicating the EDS area analysis; (b) SEM micrograph showing an α_2/γ lamellar colony with red and blue rectangles indicating the EDS area analysis; (c) elemental maps of Ti, Al and Cr collected from a region that contains the PPBs (Color figure online).

on average for the pillar structure in the post-HIP condition. This seems to suggest a slight Al gradient existed between the composite structure and its surroundings through selective Al evaporation during the SEBM process.

Figure 9 shows the wafer microstructure in the as-SEBM (Figures 9(a) and (b)) and post-HIP

(Figures 9(c) and (d)) conditions. The cross-sectional view of the wafer structure in as-SEBM condition reveals that its width varied from 539.0 to 716.3 μm and powders were attached to its arms, Figure 9(a). The high-magnification SEM micrograph in Figure 9(b) provides more detailed information. In this case, the attached powder was an AA type, given the presence of

Table III. Summary of SEM + EDS Results

Selected Areas for EDS Analysis as Indicated in Fig. 7	Chemical Composition (At. Pct)			
	Ti	Al	Nb	Cr
Capsule	49.4	46.6	2.0	2.0
Inner Area	48.6	47.5	2.1	1.8
Lamellar Grain	52.9	43.6	0.9	2.7
Coarse γ -Grains	48.3	47.8	2.1	1.9
Fine γ -Grains with PPBs	48.9	47.0	2.1	2.0

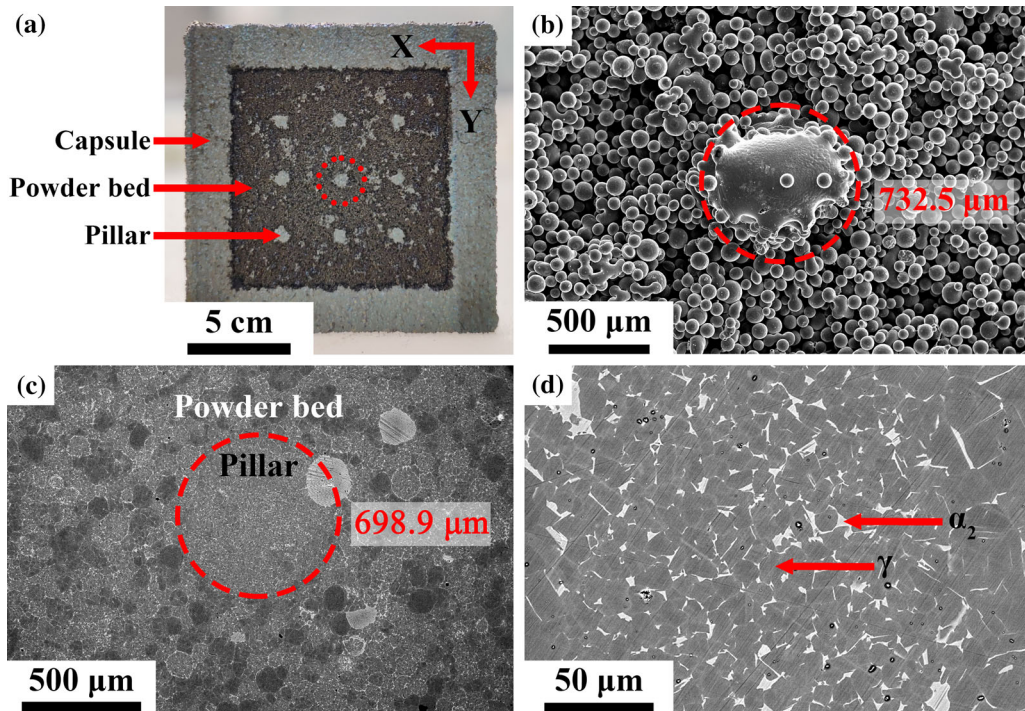


Fig. 8—Pillar composite structure: (a) photograph of the cross-sectional view in as-SEBM condition; (b) SEM micrograph showing the powder bed where the pillar region is indicated with red dotted circle; (c) and (d) SEM micrographs of the cross-sectional view in post-HIP condition with the red dotted circle indicating the pillar region (Color figure online).

internal gas pore. Also, a clearly defined PPBs can be found at the powder boundary, as indicated by the red arrow in Figure 9(b). For the post-HIP condition, the wafer microstructure was characterized by the fine equiaxed γ -grains ($9.1 \pm 5.6 \mu\text{m}$ in size, 89.5 pct in volume fraction) and α_2 -grains distributed at the γ -grain boundary, Figures 9(c) and (d). Such characteristic microstructure and phase constitution in the wafer structure were similar to the pillar structure (Figure 8(d)). The Al concentration for the wafer structure in the post-HIP condition was measured to be 46.7 ± 0.2 at. pct on average, which was again similar to the pillar structure (46.8 ± 0.4 at. pct).

For the partial-melt structural design, every two adjacent layers were supposed to form a cross-hatch pattern, ultimately in three-dimensional space creating 36 partitions when viewed from the top. This has been confirmed to be the case for the as-SEBM condition, see the inset of Figure 10(a). The partial-melt structure as

well as the attached powders are illustrated in Figure 10(a), from which SEM image was taken to reveal their microstructure details as shown in Figure 10(b). For the powder 1 in Figure 10(b), it consisted of fine γ -grains and the Al content was measured to be 47.1 at. pct by EDS, whereas the powder 2 consisting of coarse γ -grains contained a higher Al content of 49.1 at. pct. Recall that the AA powder had a lower Al than the PREP powder (Figure 2(b)). This means that powder 1 was AA type while powder 2 was PREP type.

Figures 10(c) and (d) present the partial-melt structure in the post-HIP condition. First, a clearly defined boundary can be seen between the partial-melt region with a typical width of $400 \mu\text{m}$ and the densified powder bed, as indicated by the red dash lines in Figure 10(c). The high-magnification SEM in Figure 10(d) reveals that the microstructure of the partial-melt was characterized by the fine equiaxed γ -grains ($12.3 \pm 7.0 \mu\text{m}$ in

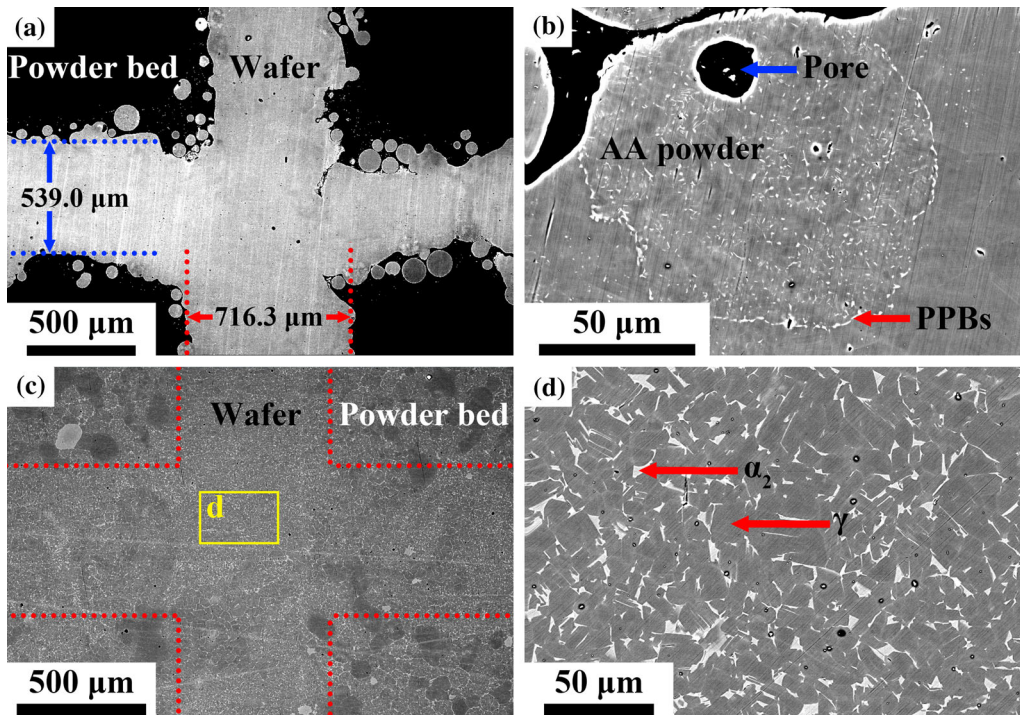


Fig. 9—Wafer composite structure: (a) SEM micrograph of the cross-sectional view in as-SEBM condition; (b) SEM micrograph showing the attached powder to wafer; (c) and (d) SEM micrographs of the cross-sectional view in the post-HIP condition, with red dotted lines delineating the boundary between the wafer and powder bed (Color figure online).

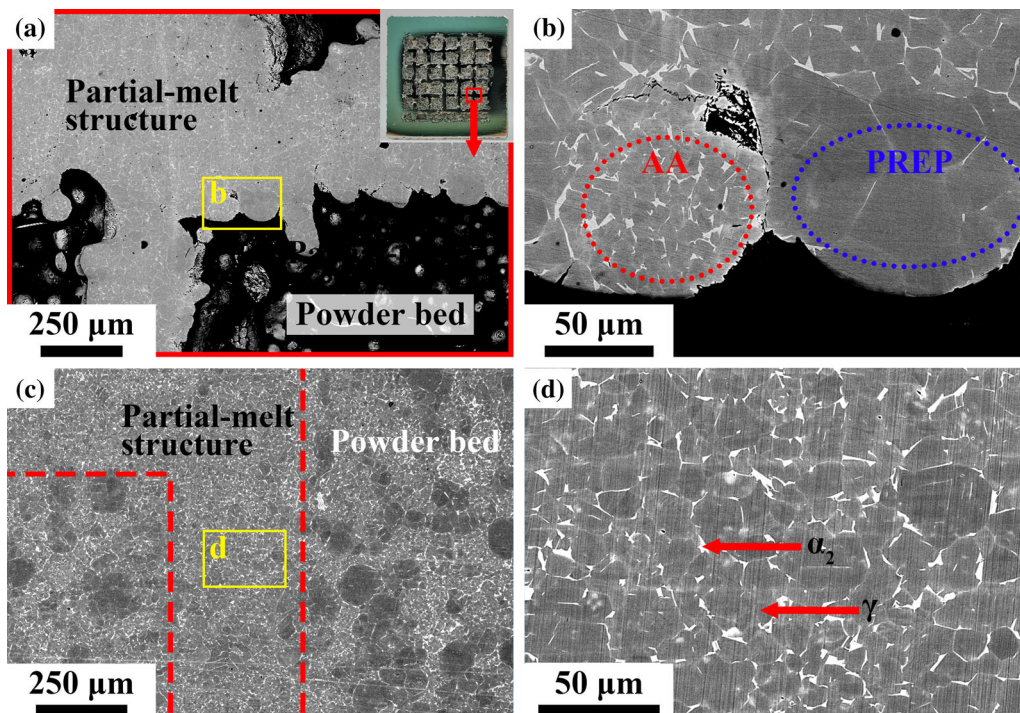


Fig. 10—Partial-melt composite structure: (a) SEM micrograph of the cross-sectional view in as-SEBM condition together with the inset providing the overview; (b) SEM micrograph showing the microstructure of the attached powder, with the dotted circles indicating EDS analysis area; (c) and (d) SEM micrographs of the cross-sectional view in post-HIP condition, with the red dotted lines indicating the pillar region (Color figure online).

size, 92.7 pct in volume fraction) and the irregular-shaped α_2 -grains distributed at the γ -grain boundaries. The Al concentration was measured to be

46.3 ± 0.2 at. pct on average for the partial-melt structure in the post-HIP condition, resulting in the Al loss of 2.1 at. pct, which was marginally higher than that

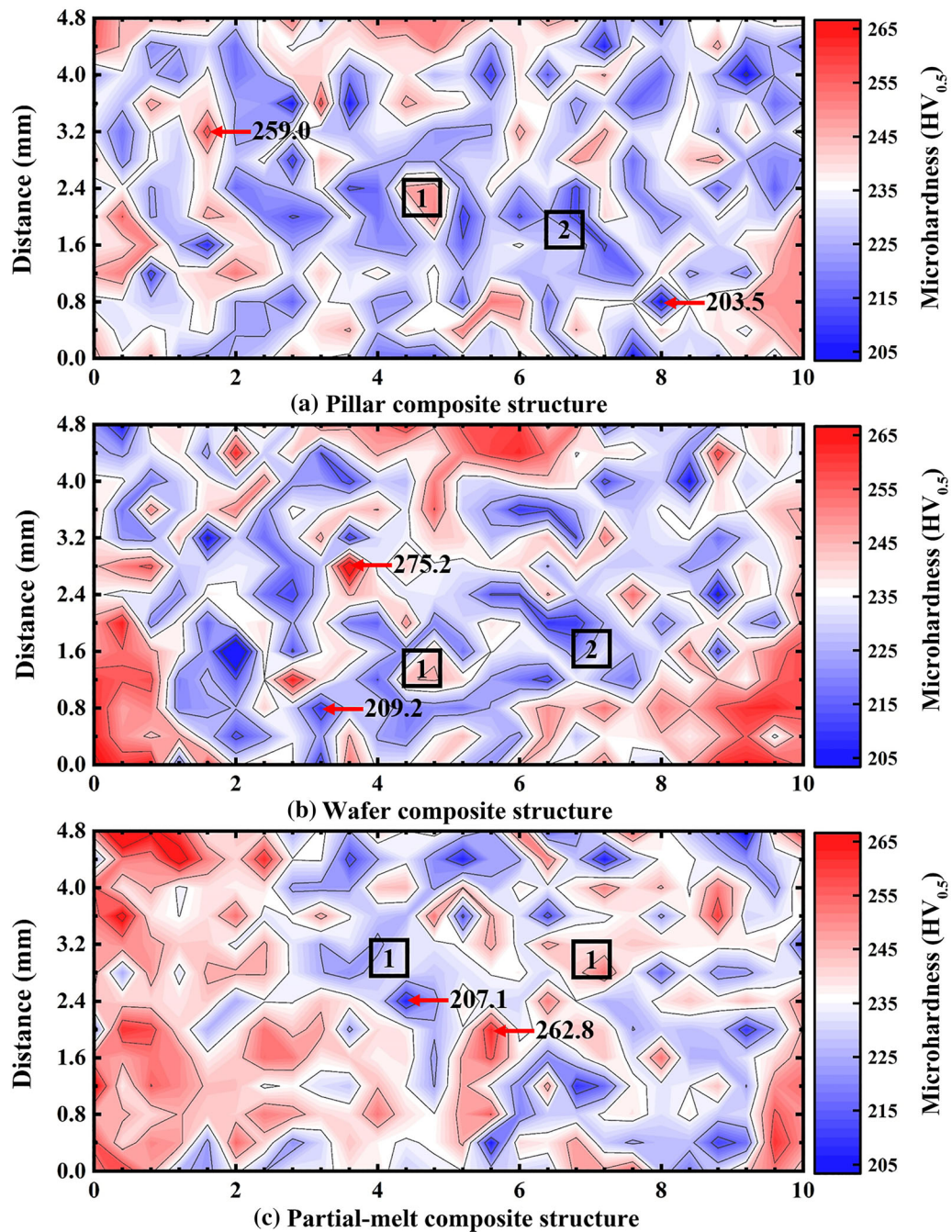


Fig. 11—Microhardness maps for the pillar, wafer and partial-melt composite structures, with the left and right sides situated within the capsule and the inner area in-between.

of 1.8 at. pct in wafer structure. This can be attributed to the lower scan speed used for processing the partial-melt structure compared to the wafer structure (1200 mm/s vs. 2000 mm/s in Table I).

D. Microhardness

A significant microstructure difference was observed between the powder bed area and *in-situ* composite structure in the post-HIP condition, Figures 8(c) (pillar), 9(c) (wafer) and 10(c) (partial-melt). Thus,

microhardness mapping was performed to evaluate the location-specific mechanical property of the SEBM capsule. The $HV_{0.5}$ hardness distribution within the horizontal cross-section of the pillar sample is illustrated in Figure 11(a), including both the left and right sides of the capsule as well as the inner area in-between. The highlighted area 1 in Figure 11(a) represented a typical pillar region with a hardness of $244.2 \pm 9.0 HV_{0.5}$, whereas area 2 was likely to be the powder bed region with a lower hardness of $224.3 \pm 7.3 HV_{0.5}$. The capsule area had the highest hardness of $248.7 \pm 2.0 HV_{0.5}$.

Overall, the high hardness of the capsule and pillar areas can be attributed to the fine γ -grain microstructure as observed in Figures 6(b) and 8(d). The higher volume fraction of the α_2 -phase with signs of incipient lamellar γ/α_2 colony in the capsule area (Figure 6(b)) explains reasonably well for the highest hardness. However, there was evidence to suggest that other microstructural factors (e.g. the lamellar colony), can also elevate the local hardness value. Therefore, the fine γ -grains might not be the sole reason for interpreting the soft and hard regions as revealed in the hardness map.

In terms of the wafer structure, local variation of the hardness can be seen in Figure 11(b), with the wafer area (e.g., area 1 in Figure 11(b)) having an average hardness of 238.9 ± 10.2 HV_{0.5}. By comparison, the soft region (e.g., area 2 in Figure 11(b)) representing the powder bed had a hardness of 222.0 ± 7.9 HV_{0.5}. For the partial-melt structure, the average hardness as measured in the partial-melt and the powder bed regions were 243.8 ± 5.5 and 229.2 ± 4.1 HV_{0.5} (with area 1 and 2 in Figure 11(c) representing the regions), respectively.

E. Post-heat Treated Condition of the Bulk Sample

The post-HIP samples were subjected to heat treatment at 1350 °C for 30 minutes, followed by step cooling as described in Section II-A, with the aim to obtain the lamellar microstructure. Figure 12 shows the microstructure of the wafer structure in the post-HT condition. For the capsule area, the microstructure transformed from a duplex type with equiaxed γ -grains as the primary (size of 7.5 ± 4.4 μm , volume fraction of 86.3 pct, Figure 6(b)) to a nearly lamellar type (colony

size of 143.1 ± 102.7 μm , volume fraction of 77.9 pct, Figures 12(a) and (b)). The high-magnification SEM micrograph (Figure 12(b)) suggests that the transition from the equiaxed γ -grains to lamellar microstructure was not yet completed. Some remaining γ -grains, as indicated by the red arrow in Figure 12(b), can be found in the regions near the lamellar α_2/γ colony boundary.

In terms of the inner area of the wafer sample, a rather complex microstructure was seen in the typical powder bed region, Figure 12(c). The microstructure was characterized by the larger lamellar colonies (colony size of 76.9 ± 38.1 μm , volume fraction of 16.6 pct), the smaller equiaxed γ -grains (size of 12.2 ± 9.7 μm , volume fraction of 63.6 pct) and the irregular-shaped α_2 -grains (volume fraction of 19.8 pct). Some interconnected lamellar colonies with considerably large size of > 500 μm also appeared, Figure 12(d), probably due to the wafer structural design, but their presence was rare. Overall, the wafer composite structure could not survive from the heat treatment. However, no PPBs were found in the inner area, suggesting that heat treatment is beneficial in terms of eliminating the PPBs.

SEM observation of the inner area of the pillar sample in the post-HT condition is shown in Figure 13(a), which looks similar to the wafer structure in Figures 12(c) and (d). The interconnected lamellar colonies, outlined by the red dotted circle with a diameter of 807 μm in Figure 13(a), were likely inherited from the pillar structure. By comparison, the densified powder bed region consisted of α_2/γ lamellar colonies (colony size of 64.6 ± 38.4 μm , volume fraction of 23.5 pct) and equiaxed γ -grains (size of 19.2 ± 14.7 μm , volume fraction of 66.5 pct).

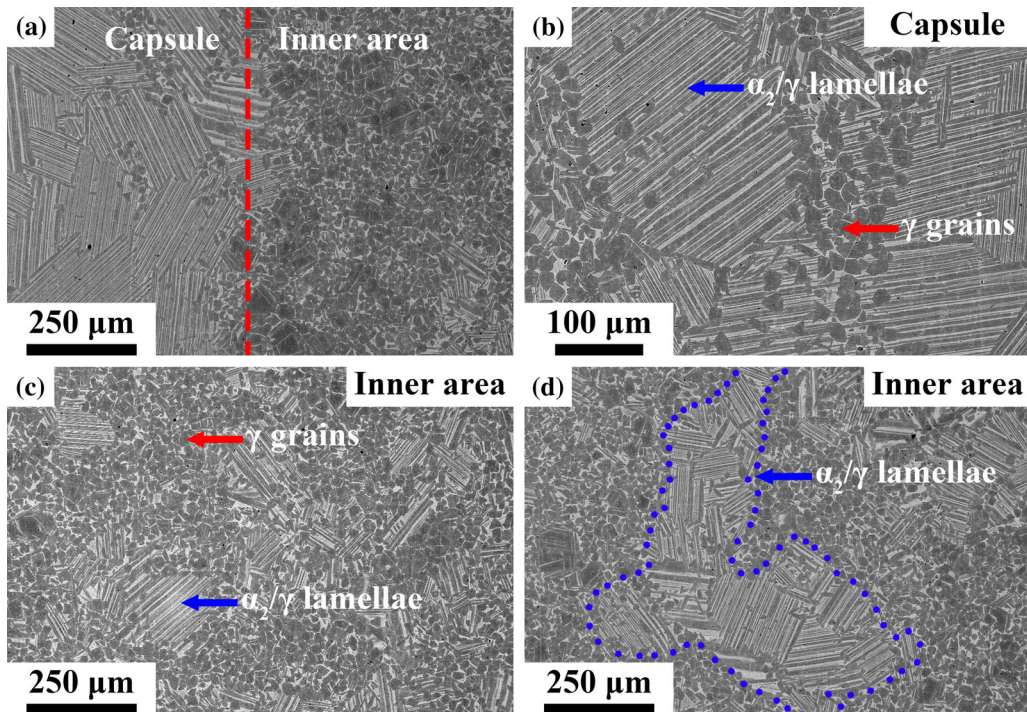


Fig. 12—SEM micrographs of the cross-sectional view of wafer sample in the post-HT condition: (a) overall microstructures in the capsule and inner areas; (b) detailed microstructure of the capsule area; (c) and (d) detailed microstructure of the inner area.

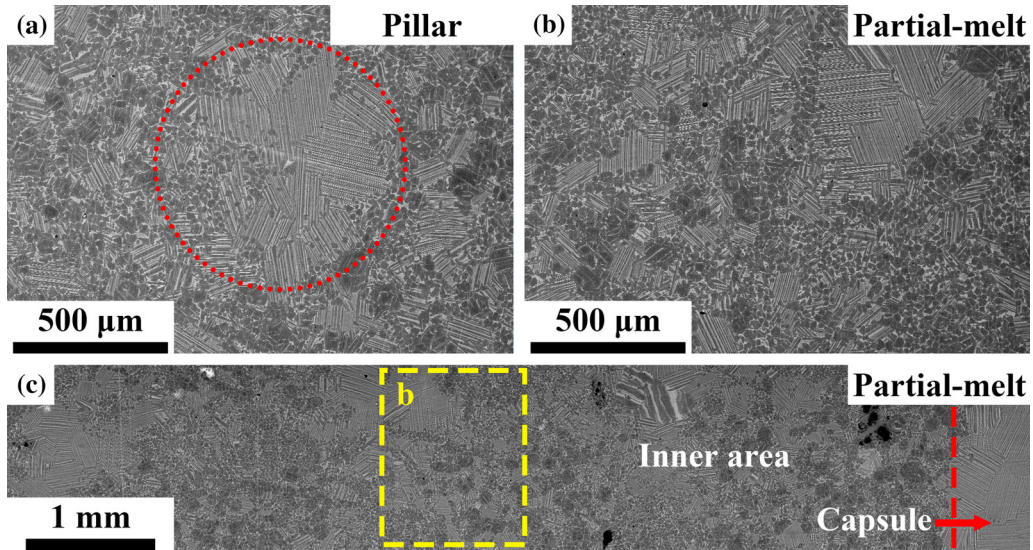


Fig. 13—SEM micrographs of the horizontal cross-sectional view of the pillar structure in (a) and partial-melt structure in (b) as observed in the post-HT condition; (c) a low-magnification SEM micrograph showing the duplex microstructure in the inner area of the partial-melt structure.

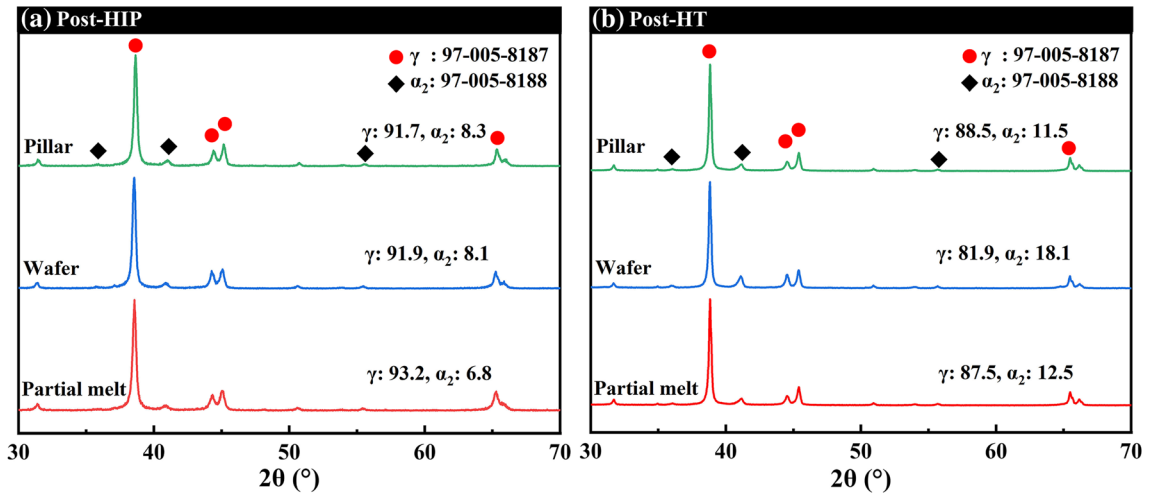


Fig. 14—XRD spectra of the pillar, wafer and partial-melt composite structures: (a) post-HIP condition; (b) post-HT condition.

The microstructure of the partial-melt sample in the post-HT condition is shown in Figure 13(b) and (c), where the boundary between the partial-melt structure was less defined. Overall, the microstructure of the partial-melt sample consisted of a relatively high volume fraction of α_2/γ lamellar colonies (colony size of $69.0 \pm 46.5 \mu\text{m}$, volume fraction of 35.5 pct) with equiaxed γ -grains (size of $23.9 \pm 12.9 \mu\text{m}$, volume fraction of 51.8 pct) as the remainder. This might be attributed to the large volume fraction of the melted area under this composite structure, creating a higher Al loss of 2.1 at. pct (0.5 at. pct higher than pillar sample). The higher Al loss would decrease the α -transus temperature, promoting the equilibrium content of α -phase at heat treatment temperature.

XRD phase identification was performed on all three composite structures in the post-HIP and post-HT conditions and the results are summarized in Figure 14. In the post-HIP condition, their microstructure consisted of mainly γ -phase with the volume fraction of higher than 90 pct, Figure 14(a). Overall, this finding is consistent with the SEM-based analysis presented in Section 3.3, in which the pillar, wafer and partial-melt contained 86.3, 89.5 and 92.7 pct γ -grains, respectively. After the heat treatment, the volume fraction of α_2 -phase increased to 11.5, 18.1 and 12.5 pct, for the pillar, wafer and partial-melt composite structures, respectively, Figure 14(b). Again, this finding is consistent with the SEM observation of the post-HT samples revealing a high volume fraction of α_2/γ lamellar colonies (Figures 12 and 13).

IV. DISCUSSION

A. Microstructure Formation Mechanisms in Post-HIP Condition

The triple microstructure as observed in the inner area of the post-HIP condition, Figures 6(c) and (d), consists of the fine γ -grains with shell-like PPBs, coarse γ -grains without the PPB, and the circular lamellar α_2/γ colonies. Such a complex microstructure deserves an in-depth discussion about their formation mechanisms. According to the literature,^[21,22] the fine γ -grains with PPBs are a typical microstructure in TiAl after HIP. Such microstructure was also found in high Nb–TiAl^[19] and TNM TiAl^[31] fabricated by spark plasma sintering (SPS).

The formation mechanism of the fine γ -grains inside the PPBs can be attributed to the AA powder that is characterized by the dendrite segregation (Figure 2(f)). Note that the coarse dendritic structure in the AA powder was also mentioned in several TiAl studies.^[18,31–34] The phase constitution of the AA powder contains 98.3 pct of the metastable α_2 -phase (XRD result in Figure 3), a non-equilibrium TiAl microstructure due to rapid solidification during the powder production (*i.e.* Ar gas atomization). This aligns well with the previous study using the AA powder made of Ti–48Al–2Cr–2Nb (96 pct α_2 -phase) [34] and TNM (85.6 pct to 93.5 pct α_2 -phase).^[33] Guyon *et al.*^[34] found that the metastable α_2 -phase dendrites of the AA powder decomposed into γ -grains with fine acicular α_2 -precipitates at the temperature range from 675 °C to 875 °C during the differential thermal analysis measurement. Likewise, Kastenhuber *et al.*^[33] reported such phase decomposition in TNM TiAl powder due to high-temperature exposure at \sim 700 °C. It is thus believed that during the long-term thermal exposure of the SEBM (1050 °C) and HIP (1250 °C), the metastable coarse α_2 -phase dendrites of the AA powder would be transformed into fine γ -grains.

The above-mentioned phase transformation may involve the following sequence of nano-lamellae transformation from the α_2 -phase according to the Blackburn orientation relationship, followed by recrystallization to γ -grains with the nucleation appearing preferentially at the lamellar colony boundaries and the interface between α_2 and γ lamellae.^[35] Our XRD spectra of mixed and recycled powders (Figure 3) provide the evidence, given that a significantly reduced α_2 -phase fraction of 14.9 pct was found in the recycled powder (thermal exposure at 1050 °C for \sim 4 hours per machine cycle), when compared to that 67.4 pct in the mixed powder (without seeing SEBM thermal exposure)

For the PPBs surrounding the fine γ -grains, they are composed of the fine α_2 -grains with a well-defined Al depletion (Figure 7(c)). Oxygen or nitrogen absorbed to the powder surface was claimed as the reason for the formation of PPBs in PM TiAl.^[19] The nano-scale layer with oxygen enrichment was observed in both the AA (40 nm^[21] and 54 nm^[36] thick) and PREP (10 nm thick^[19]) TiAl powders. Since oxygen in TiAl is a strong

α -phase stabilizer,^[37] it seems to explain well about the phase constitution of PPBs.

However, Bieske *et al.*^[21] found that the virgin TiAl powder that had not experienced the SEBM cycle did not reveal the PPBs after the HIP process, despite the oxygen enriched layer at the powder surface. By contrast, the PPBs appeared in the recycled powder. Given that little oxygen difference was found by comparing the virgin *vs.* recycled powders using X-ray photoelectron spectroscopy, the formed PPBs cannot be attributed to oxygen absorption at the powder surface after being subjected to the SEBM cycle. Instead, their electron probe microanalysis result revealed an Al concentration gradient with the powder surface being depleted in Al while the interior being rich.^[21] Therefore, the defocused beam used in the SEBM pre-heat step was believed to cause the local evaporation of Al in the powder. Our present EDS observation in Figure 7(c) seems to suggest the same reason for the PPBs formation (*i.e.* Al depletion).

In fact, the Al lean region can be linked to the primary α_2 -phase in the PPBs on the basis of the TiAl phase diagram as shown in Figure 15.^[38] With the Al decreasing (red arrow in Figure 15), the α -phase fraction increases at high temperatures. This can satisfactorily explain why the Al-depleted layer near the powder surface exhibits a much higher α_2 -phase fraction. Furthermore, the SEM micrograph in Figure 9(b) confirms that the PPBs are developed during the SEBM preheat step. The PPBs near the powder surface in the AA powder in the post-HIP condition, *i.e.* heat treatment of the nascent powder at 1250 °C for 4 hours without the high pressure (Figure 5(b)), also supports this

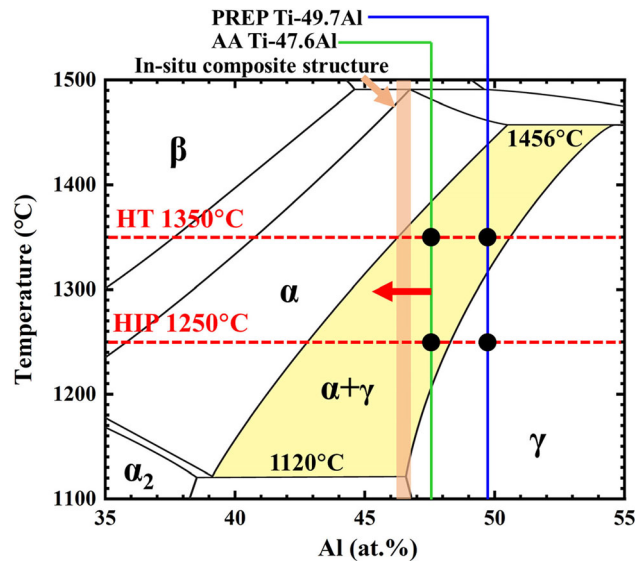


Fig. 15—Section of the binary TiAl phase diagram highlight the $\alpha + \gamma$ region. The red dashed lines indicate the HIP temperature of 1250 °C and the heat treatment temperature of 1350 °C. The blue and green lines indicate the chemical composition of the PREP and AA powders. The solid filled region by orange indicates the composition range of *in-situ* composite structures. Note that phase boundaries of the TiAl phase diagram are obtained from Ref. [38] (Color figure online).

interpretation. Thus, the Al evaporation at the powder surface during the SEBM preheat step is the main reason for the formation of PPBs surrounding the fine γ -grains.

Now let's consider how the powder microstructure evolves into the one characterized by the coarse γ -grains without the PPB (blue dotted circle in Figure 6(d)). According to the EDS results in Figure 7 and Table III, the Al concentration in the coarse γ -grains is higher than the fine γ -grains. Given the compositional difference between the PREP (49.66 at. pct) and AA (47.61 at. pct) powders being ~ 2 at. pct (Figure 2(b)), one plausible explanation is that the coarse γ -grains originate from the PREP powder. This indeed agrees with the EDS result on the coarse γ -grains of the partial-melt sample (region 2 in Figure 10(b)), showing the high Al of 49.1 at. pct which is very close to the composition of the nascent PREP powder. Also, the EDS analysis performed on the post-HIP powders as shown in Figure 5(e) provides additional evidence to support this hypothesis.

Figure 15 shows the equilibrium phase diagram of TiAl alloy together with the green and blue lines indicating the AA and PREP powder compositions, respectively. The PREP powder with composition of Ti-49.66Al-1.89Nb-2.00Cr is in the single γ -phase zone at the HIP temperature of 1250 °C, while the AA powder with the composition of Ti-47.61Al-2.00Nb-1.97Cr is in the two-phase ($\alpha + \gamma$) zone. This means that the γ -phase grains inherited from the PREP powder can grow during the thermal exposure at 1250 °C for 4 hours. But, the presence of α_2 -grains in the AA powder seems to prevent the γ -grain growth, resulting in a fine γ -grain microstructure. The lack of PPBs in the coarse γ -grains implies that their formation can be avoided by increasing the Al concentration in the pre-alloyed TiAl powder. An attempt was made using the differential scanning calorimetry (DSC) with the nascent AA and PREP powders to establish the accurate $\alpha_2 + \gamma \rightarrow \gamma$ transition temperatures. Unfortunately, it was unable to separate the $\alpha_2 + \gamma \rightarrow \gamma$ DSC characteristic peak from the heating curves (Figure A1). This might be caused by the exothermic peak which kicks in at ~ 900 °C and above (refer to Appendix for more details).

The third characteristic feature of the triple microstructure is the circular lamellar α_2/γ colonies, see the yellow dotted outline in Figure 6. Since their size of 233.5 μm clearly exceeds the D90 of the mixed powder (143 μm), it is difficult to attribute their formation to the individual powder type (AA or PREP). Also, it does not seem that this microstructure is a result of HIP process because the circular lamellae contain Al of 43.6 at. pct and Nb of 0.9 at. pct, which are considerably lower than the powder (48.41 at. pct Al and 1.96 at. pct Nb), Table III.

The powder collected from the sieve residuals as shown in Figure 4, together with EDS determined composition, suggests that the powder edges are rich in Al (points 2 and 3), while the central area is lean in Al (points 1 and 4). It is thus hypothesized that their presence is owing to the splashed droplet.^[39,40] Due to electrostatic repulsion action of the electron beam, it is likely that some partially or completely melted droplets fly out from the powder bed. The surface of the flown

droplet causes Al evaporation to the vacuum chamber, leading to the formation of Al gradient with the lower Al concentration at the surface. The splashed droplet would eventually fall back onto the powder bed, and the Al-depleted region at the surface is quickly solidified to form the fine-grained microstructure. In contrast, the high Al-rich part is solidified with a slower rate, forming the coarser microstructure. The reason why the local Al loss near the surface of the attached powder is considerably high (~ 6 at. pct as measured by points 1 and 4 in Figure 4) can be attributed to the much larger specific surface area of the droplet when compared to the molten pool. Some of the splashed droplets may have been solidified before falling back onto the powder bed. During the HIP process, these droplets would be subjected to a phase transformation into α -phase at 1250 °C if the Al concentration is low enough (*i.e.* lower than the value of 42.5 at. pct, Figure 15), followed by the phase transformation into the lamellar colony upon cooling. The EDS result on the post-HIP sample (Table III) corroborates our hypothesis in a sense that a significant Al loss is associated with the circular lamellar colonies.

B. In-situ Composite Structural Design

Using the soft material as the matrix to give the ductility while the hard one providing the strength is a widely adopted approach in materials science, *e.g.* the carbon fiber reinforced polymer^[41] and Nb-silicide composite material.^[42] For the latter, due to the intrinsic poor room temperature ductility and toughness of the hard Nb₅Si₃ phase, the soft phase of Nb solid solution has been designed to improve toughness.^[43]

In the present work, the *in-situ* composite structural design (pillar, wafer and partial-melt in Figures 1(b) to (d)) *via* SEBM capsule technology has been explored. TiAl alloy has been chosen as the candidate material as its microstructure is highly sensitive to the Al concentration.^[1,4,37] This offers the potential to manipulate the Al evaporation by selectively melting the material *via* electron beam. For the pillar, wafer and partial-melt regions in the post-HIP condition, the Al concentration was 46.8, 46.7 and 46.3 at. pct, respectively. This means that at 1250 °C (HIP temperature in Figure 15), these composite structures are within the two-phase ($\gamma + \alpha$) zone. This results in the formation of fine equiaxed γ -grains with the α_2 -phase at the boundary in the post-HIP condition (Figures 8(d), 9(d) and 10(d)). The γ -grain size in the wafer, pillar and partial-melt structure was measured to be 9.1 ± 5.6 , 10.5 ± 6.6 and 12.3 ± 7.0 μm , which is smaller than the densified powder bed area (20.7 ± 14.1 μm). This might be one of the reasons responsible for the elevated hardness, namely, the harder region associated with the composite structure (Figure 11), according to the Hall-Petch relationship.^[44,45]

The location-specific Al loss due to the selective Al evaporation results in the decreased γ to α transition temperature. In theory, this means that in the bulk sample, with the tightly controlled heat treatment temperature, some regions can be at the fully lamellar or nearly lamellar temperature window while the other

regions are within the equiaxed- γ window. Unfortunately, in practice, all the composite structures characterized by the equiaxed- γ microstructure are transformed into larger interconnected lamellar colonies as observed in the post-HT condition (Figures 12(d) and 13(a)). This means that the composite structure could not survive from the heat treatment.

The considerable Al loss in the composite structure combined with the higher heat treatment temperature (1350 °C vs. 1250 °C) means that the material is more towards the single α -phase region, as highlighted by the orange area in Figure 15. This seems to explain why the final microstructure is characterized by the partially transformed lamellar type with γ -grains at the lamellar $\alpha_2 + \gamma$ colony boundary. Also, the self-diffusion rate at 1350 °C would be approximately one order of magnitude faster compared to 1250 °C,^[46] which helps to reduce the local Al gradient. It is obvious that the large vertical interface between the inner area and capsule facilitates the directional Al diffusion path with the inner area being the high Al region. Thus, a full lamellar transformation occurs in the capsule (Figure 12(a)). The multiple composite structures would equally consume the adjacent Al-rich region without any directionality, and thus the fully lamellar transformation process could not be completed. Two future directions are thus recommended. Post-HIP heat treatment temperature needs to be further optimized, and a higher beam current might be employed to create a greater Al gradient within the powder bed area (composite structure vs. the remainder of powder bed).

The lower density of the samples (Table II) in the as-SEBM condition might be caused by the vacuum pressure of 1 Pa. The SEBM chamber was firstly pumped to a vacuum pressure of 1×10^{-3} Pa, followed using the high-purity helium to regulate the pressure to 0.1 or 1 Pa in order to prevent the smoke phenomenon.^[3,24] By contrast, the powder-filled capsule in a conventional HIP process would be sealed under high vacuum levels (1×10^{-3} Pa,^[47] 6.5×10^{-4} Pa^[48]). Thus, the regulating gas during the SEBM process can be entrapped inside the capsule, which becomes difficult to be removed during the HIP process.^[49-51] Future work is needed to investigate the effect of pores on mechanical properties.

V. CONCLUSIONS

The following conclusions can be drawn:

- (1) *In-situ* composite structural design of gamma-TiAl over the millimeter sample dimension is realized using a combinational PM approach of SEBM and HIP. The microstructure evolution from the powder to bulk sample has been tracked successfully using the mixed powder with the higher (PREP type) and lower (AA type) Al concentrations.
- (2) The AA powder containing the lower Al concentration transforms into the fine γ -grains with PPBs, and the α -phase at the boundaries helps to

prevent the growth of γ -grains at elevated temperatures. By comparison, the PREP powder with higher Al transforms into coarse γ -grains without the PPBs because the composition would locate the material within the single γ -phase region at the chosen HIP temperature of 1250 °C.

- (3) The inner area of the SEBM capsule is characterized by a unique triple microstructure in the post-HIP condition: coarse γ -grains, fine γ -grains with PPBs and circular lamellar colonies. The higher Al powder (49.66 at. pct) is responsible for the coarse γ -grains, while the lower Al powder (47.61 at. pct) is associated with the fine γ -grains with the PPBs. The splashed droplet due to the SEBM process is likely to be responsible for the large circular lamellar colonies.
- (4) For the PPBs surrounding the fine γ -grains, their microstructure is characterized by the fine α_2 -grains with a clearly defined Al-depleted region. The PPBs can be eliminated by increasing the Al concentration of the raw powder as evidenced using the higher Al powder.
- (5) No PPBs was found in the inner area of the bulk sample after the heat treatment at 1350 °C, suggesting that the heat treatment is beneficial in terms of eliminating the PPBs. However, the composite structure cannot survive from it.

ACKNOWLEDGMENTS

HP acknowledges financial support from National Science and Technology Major Project (Grant No. 2019-VII-0016-0157) and National Natural Science Foundation of China (Grant No. 51831001). BC acknowledges financial supports from the UK's Engineering and Physical Sciences Research Council, EPSRC First Grant Scheme (Grant No. EP/P025978/1) and Early Career Fellowship Scheme (Grant No. EP/R043973/1), and from the British Council, Newton Fund Researcher Links Grant Agreement ID 2020-RLWK12-10091. A special thank you is given to Prof. Sheng-kai Gong at Beihang University who initiated this long-lasting research collaboration between HP and BC.

OPEN ACCESS

This article is licensed under a Creative Commons Attribution 4.0 International License, which permits use, sharing, adaptation, distribution and reproduction in any medium or format, as long as you give appropriate credit to the original author(s) and the source, provide a link to the Creative Commons licence, and indicate if changes were made. The images or other third party material in this article are included in the article's Creative Commons licence, unless indicated otherwise in a credit line to the material. If material is not included in the article's Creative Commons licence

and your intended use is not permitted by statutory regulation or exceeds the permitted use, you will need to obtain permission directly from the copyright holder. To view a copy of this licence, visit <http://creativecommons.org/licenses/by/4.0/>.

APPENDIX: DIFFERENTIAL SCANNING CALORIMETRY (DSC)-BASED $\alpha_2 + \gamma \rightarrow \gamma$ TRANSITION TEMPERATURE DETERMINATION

The phase transformation temperatures of both the AA and PREP powders were studied using the DSC technique on a Netzsch STA 449F3 instrument. The DSC measurements from the room temperature to 1350 °C, under the heating and cooling rate of 10 K/min,

were performed in alumina crucible using a dynamic argon atmosphere with a flow rate of 50 mL/min. Figure A1(a) shows the overall heating and cooling curves of the AA and PREP powders. The DSC curve of the AA powder (Figure A1(b)) during the heating step exhibited an exothermic peak between 650 °C and 750 °C, indicating the transformation of the metastable α -phase formed during the atomization process to its equilibrium condition.^[33,34,52,53] This is consistent with the absence of such a peak during the subsequent cooling step of the AA powder, Figure A1(a). The DSC curve of the PREP powder (Figure A1(b)) during the heating step also presented an exothermic peak between 610 °C and 750 °C but with a weaker intensity. This is consistent with the XRD results (Figure 3), in which the AA powder (98.3 pct) consisted of higher volume fraction of the metastable α -phase than PREP powder (44.4 pct).

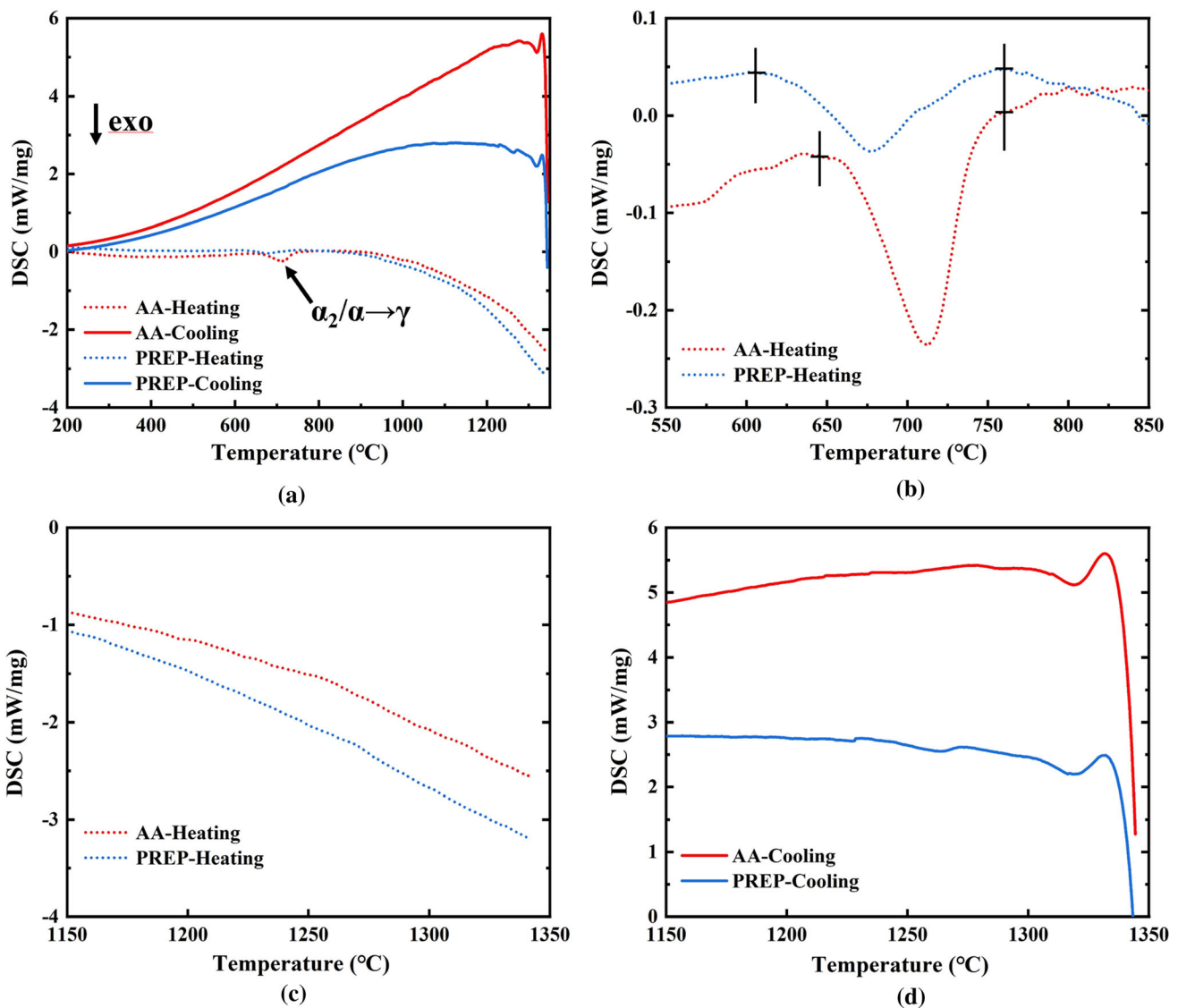


Fig. A1—DSC curves of the AA and PREP powders: (a) overall DSC curves during heating to, and cooling from 1350 °C, both under the rate of 10 °C/min; (b) enlarged view of the middle-temperature range showing the heating step; (c) and (d): heating and cooling curves of AA and PREP powder at temperature range from 1150 °C to 1350 °C.

Unfortunately, it was unable to separate the $\alpha_2 + \gamma \rightarrow \gamma$ DSC characteristic peak from the heating curves as shown in Figure A1(c), nor from the cooling curves of Figure A1(d). This might be attributed to the exothermic process which kicks in at ~ 900 °C. Previous work by Kastenhuber^[33] suggested the presence of a recrystallization process at inter-dendritic areas of gas atomized TiAl powder when it was annealed over 600 °C. According to the XRD spectra, the recrystallization process started at 700 °C and the resulting γ -phase fraction increased with ascending annealing temperature. In addition, the recrystallization process usually leads to the exothermic peak in the DSC curve, due to the stored energy release.^[54–56]

REFERENCES

- J. Schwerdtfeger and C. Körner: *Intermetallics*, 2014, vol. 49, pp. 29–35.
- L.E. Murr, S.M. Gaytan, A. Ceylan, E. Martinez, J.L. Martinez, D.H. Hernandez, B.I. Machado, D.A. Ramirez, F. Medina, S. Collins, and R.B. Wicker: *Acta Mater.*, 2010, vol. 58, pp. 1887–94.
- R. Gao, H. Peng, H. Guo, and B. Chen: *Scr. Mater.*, 2021, vol. 203, 114092.
- M. Todai, T. Nakano, T. Liu, H.Y. Yasuda, K. Hagihara, K. Cho, M. Ueda, and M. Takeyama: *Addit. Manuf.*, 2017, vol. 13, pp. 61–70.
- D. Cormier, O. Harrysson, T. Mahale, and H. West: *Res. Lett. Mater. Sci.*, 2007, vol. 2007, pp. 1–4.
- H. Yue, Y. Chen, X. Wang, S. Xiao, and F. Kong: *J. Alloys Compd.*, 2018, vol. 766, pp. 450–59.
- W. Kan, B. Chen, H. Peng, Y. Liang, and J. Lin: *Mater. Lett.*, 2020, vol. 259, p. 1268.
- W. Kan, B. Chen, C. Jin, H. Peng, and J. Lin: *Mater. Des.*, 2018, vol. 160, pp. 611–23.
- H. Yue, Y. Chen, X. Wang, and F. Kong: *J. Alloys Compd.*, 2018, vol. 750, pp. 617–25.
- A. Powell, J. Van Den Avyle, B. Damkroger, J. Szekely, and U. Pal: *Metall. Mater. Trans. B*, 1997, vol. 28B, pp. 1227–39.
- H.P. Tang, G.Y. Yang, W.P. Jia, W.W. He, S.L. Lu, and M. Qian: *Mater. Sci. Eng. A*, 2015, vol. 636, pp. 103–07.
- M. Seifi, A.A. Salem, D.P. Satko, U. Ackelid, S.L. Semiatin, and J.J. Lewandowski: *J. Alloys Compd.*, 2017, vol. 729, pp. 1118–35.
- W. Kan, B. Chen, H. Peng, Y. Liang, and J. Lin: *J. Alloys Compd.*, 2019, vol. 809, pp. 1–32.
- S.L. Semiatin, G.R. Cornish, and D. Eylon: *Mater. Sci. Eng. A*, 1994, vol. 185, pp. 45–53.
- K. Frkáňová and J. Lapin: *Conf. Metall. Mater.*, 2012, vol. 2012, pp. 1227–33.
- J. Wang, Q. Luo, H. Wang, Y. Wu, X. Cheng, and H. Tang: *Addit. Manuf.*, 2020, vol. 32, p. 101007.
- A. Denquin and S. Naka: *Acta Metall. Inc.*, 1996, vol. 44, pp. 353–65.
- M. Schloffer, F. Iqbal, H. Gabrisch, E. Schwaighofer, F.P. Schimansky, S. Mayer, A. Stark, T. Lippmann, M. Göken, F. Pyczak, and H. Clemens: *Intermetallics*, 2012, vol. 22, pp. 231–40.
- H.Z. Niu, T.X. Gao, Q.Q. Sun, H.R. Zhang, D.L. Zhang, and G.L. Liu: *Mater. Sci. Eng. A*, 2018, vol. 737, pp. 151–57.
- T. Voisin, J.P. Monchoux, M. Hantcherli, S. Mayer, H. Clemens, and A. Couret: Microstructures and mechanical properties of a multi-phase β -solidifying TiAl alloy densified by spark plasma sintering. *Acta Mater.*, 2014, vol. 73, pp. 107–15.
- J. Bieske, M. Franke, M. Schloffer, and C. Köerner: *Intermetallics*, 2020, vol. 126, p. 106929.
- Y. Liu, X. Liang, B. Liu, W. He, J. Li, Z. Gan, and Y. He: *Intermetallics*, 2014, vol. 55, pp. 80–89.
- S.L. Draper and D. Isheim: *Intermetallics*, 2012, vol. 22, pp. 77–83.
- J. Jin, R. Gao, H. Peng, H. Guo, S. Gong, and B. Chen: *Metall. Mater. Trans. A*, 2020, vol. 51A, pp. 2411–29.
- Y. Yao, C. Xing, H. Peng, H. Guo, and B. Chen: *Mater. Sci. Eng. A*, 2021, vol. 802, 140629.
- G. Soundarapandiyam, C. Johnston, R.H.U. Khan, C.L.A. Leung, P.D. Lee, E. Hernández-Nava, B. Chen, and M.E. Fitzpatrick: *Addit. Manuf.*, 2021, vol. 46, 102101.
- Y. Xia, S.D. Luo, X. Wu, G.B. Schaffer, and M. Qian: *Mater. Sci. Eng. A*, 2013, vol. 559, pp. 293–300.
- G. Wegmann, R. Gerling, and F.P. Schimansky: *Acta Mater.*, 2003, vol. 51, pp. 741–52.
- R. Guo, L. Xu, J. Wu, R. Yang, and B.Y. Zong: *Mater. Sci. Eng. A*, 2015, vol. 639, pp. 327–34.
- G. Soundarapandiyam, R. Khan, C. Johnston, B. Chen, and M. Fitzpatrick: *Mater. Des. Process. Commun.*, 2021, vol. 3, pp. 1–8.
- H. Jabbar, A. Couret, L. Durand, and J.P. Monchoux: *J. Alloys Compd.*, 2011, vol. 509, pp. 9826–35.
- R. Gerling, A. Bartels, H. Clemens, H. Kestler, and F.P. Schimansky: *Intermetallics*, 2004, vol. 12, pp. 275–80.
- M. Kastenhuber, T. Klein, B. Rashkova, I. Weißensteiner, H. Clemens, and S. Mayer: *Intermetallics*, 2017, vol. 91, pp. 100–09.
- J. Guyon, A. Hazotte, and E. Bouzy: *J. Alloys Compd.*, 2015, vol. 656, pp. 667–75.
- J. Guyon, A. Hazotte, F. Wagner, and E. Bouzy: *Acta Mater.*, 2016, vol. 103, pp. 672–80.
- Y.H. Zhou, S.F. Lin, Y.H. Hou, D.W. Wang, P. Zhou, P.L. Han, Y.L. Li, and M. Yan: *Appl. Surf. Sci.*, 2018, vol. 441, pp. 210–17.
- F. Appel, J.D.H. Paul, and M. Oehring: *Gamma Titanium Aluminide Alloys: Science and Technology*, Wiley, Singapore, 2011.
- J.C. Schuster and M. Palm: *J. Phase Equilib. Diffus.*, 2006, vol. 27, pp. 255–77.
- P. Wang, H. Zhou, L. Zhang, H. Chen, X. Zhu, H. Lei, and D. Fang: *J. Alloys Compd.*, 2020, vol. 821, 153576.
- D. Gu and Y. Shen: *Mater. Des.*, 2009, vol. 30, pp. 2903–10.
- M. Altin Karataş and H. Gökkaya: *Def. Technol.*, 2018, vol. 14, pp. 318–26.
- P. Tsakiroopoulos: *Prog. Mater. Sci.*, 2022, vol. 123, 100714.
- J.H. Kim, T. Tabaru, H. Hirai, A. Kitahara, and S. Hanada: *Scr. Mater.*, 2003, vol. 48, pp. 1439–44.
- X. Tan, Y. Kok, Y.J. Tan, G. Vastola, Q.X. Pei, G. Zhang, Y.-W. Zhang, S.B. Tor, K.F. Leong, and C.K. Chua: *J. Alloys Compd.*, 2015, vol. 646, pp. 303–09.
- H. Sharma, D. Parfitt, A.K. Syed, D. Wimpenny, E. Muzangaza, G. Baxter, and B. Chen: *Mater. Sci. Eng. A*, 2019, vol. 744, pp. 182–94.
- C. Herzig, T. Przeorski, and Y. Mishin: *Intermetallics*, 1999, vol. 7, pp. 389–404.
- L. Tan, G. He, F. Liu, Y. Li, and L. Jiang: *Materials (Basel)*, 2018, vol. 11, p. 328.
- B. Sreenu, R. Sarkar, S.S.S. Kumar, S. Chatterjee, and G.A. Rao: *Mater. Sci. Eng. A*, 2020, vol. 797, 140254.
- A.R. Balachandramurthi, J. Moverare, N. Dixit, and R. Pederson: *Mater. Sci. Eng. A*, 2018, vol. 735, pp. 463–74.
- T. Kosonen, K. Kakko, and N. Raitanen: *Powder Metall.*, 2021, vol. 0, pp. 1–9.
- A. du Plessis and E. Macdonald: *Addit. Manuf.*, 2020, vol. 34, 101191.
- R.J. Schaeffer and G.M. Janowski: *Acta Metall. Mater.*, 1992, vol. 40, pp. 1645–51.
- M. Charpentier, D. Daloz, and A. Hazotte: *Kov. Mater.*, 2012, vol. 50, pp. 301–07.
- G. Benchabane, Z. Boumerzoug, I. Thibon, and T. Gloriant: *Mater. Charact.*, 2008, vol. 59, pp. 1425–28.
- C. Garcia-Cordovilla and E. Louis: *J. Mater. Sci.*, 1986, vol. 21, pp. 971–79.
- K. Kazemi-Choobi, J. Khalil-Allafi, and V. Abbasi-Chianeh: *Mater. Sci. Eng. A*, 2012, vol. 551, pp. 122–27.

Publisher's Note Springer Nature remains neutral with regard to jurisdictional claims in published maps and institutional affiliations.